High-average-power, 100-Hz-repetition-rate, tabletop soft-x-ray lasers at sub-15-nm wavelengths

Brendan A. Reagan,[1,2,*] Mark Berrill,[1,3] Keith A. Wernsing,[1,2] Cory Baumgarten,[1,4] Mark Woolston,[1,2] and Jorge J. Rocca[1,2,4]

[1]*NSF Engineering Research Center for Extreme Ultraviolet Science and Technology, Colorado State University, Fort Collins, Colorado 80523, USA*

[2]*Department of Electrical and Computer Engineering, Colorado State University, Fort Collins, Colorado 80523, USA*

[3]*Oak Ridge National Laboratory, Oak Ridge, Tennessee 37830, USA*

[4]*Department of Physics, Colorado State University, Fort Collins, Colorado 80523, USA*

(Received 31 March 2014; published 15 May 2014)

Efficient excitation of dense plasma columns at 100-Hz repetition rate using a tailored pump pulse profile produced a tabletop soft-x-ray laser average power of 0.1 mW at $\lambda = 13.9$ nm and 20 μW at $\lambda = 11.9$ nm from transitions of Ni-like Ag and Ni-like Sn, respectively. Lasing on several other transitions with wavelengths between 10.9 and 14.7 nm was also obtained using 0.9-J pump pulses of 5-ps duration from a compact diode-pumped chirped pulse amplification Yb:YAG laser. Hydrodynamic and atomic plasma simulations show that the pump pulse profile, consisting of a nanosecond ramp followed by two peaks of picosecond duration, creates a plasma with an increased density of Ni-like ions at the time of peak temperature that results in a larger gain coefficient over a temporally and spatially enlarged space leading to a threefold increase in the soft-x-ray laser output pulse energy. The high average power of these compact soft-x-ray lasers will enable applications requiring high photon flux. These results open the path to milliwatt-average-power tabletop soft-x-ray lasers.

DOI: 10.1103/PhysRevA.89.053820 PACS number(s): 42.55.Vc, 52.38.Ph

I. INTRODUCTION

The great interest in sources of bright coherent soft-x-ray radiation that has motivated the construction of free-electron lasers [1,2] (FELs) also motivates the development of more readily accessible tabletop soft-x-ray laser (SXRL) sources. Despite the significant progress recently made in both compact high-harmonic-generation-based sources [3,4] and plasma-based SXRLs [5–15], their average power is at present lower than that delivered by soft-x-ray FEL facilities [1,2]. The average power of laser-pumped SXRLs has been limited by the relatively low repetition rate of the high-energy optical wavelength pump lasers used to drive them and by low pumping efficiency. In contrast, capillary discharge lasers are capable of milliwatt average power [16,17], but currently their wavelengths are limited to values longer than 46 nm [18]. For laser-pumped soft-x-ray lasers operating in the (10–15)-nm wavelength range, thermal effects within the flash-lamp-pumped solid-state driver lasers have limited the repetition rate to 10 Hz or less, resulting in maximum average powers ranging from 1 to 20 μW [8,10]. Recently, we reported a tabletop SXRL capable of 100-Hz-repetition-rate operation, generating 0.15-mW average power on the $\lambda = 18.9$-nm line of Ni-like Mo [19], including the hour-long operation of this laser at high repetition rates [20]. Here we report the demonstration of a 0.1-mW-average-power, gain-saturated, $\lambda = 13.9$-nm soft-x-ray laser operating at 100-Hz repetition rate made possible by combining a high-energy chirped pulse amplification (CPA) infrared laser pumped by laser diodes that delivers pulses of up to 1 J of energy at this repetition rate, with a temporally tailored infrared driver laser pulse that more efficiently pumps the plasma amplifier.

The plasma amplifiers were excited by a single-shaped pump pulse. Although the use of a single pulse has been used to drive tabletop soft-x-ray lasers before [9,13,19], the pulse employed here has different characteristics. The advantage of shaping the temporal sequence of pulses used to efficiently create and heat soft-x-ray plasma amplifiers has been recognized [7,13]. In particular it was shown that the addition of a short-duration [2-ps full width at half maximum (FWHM)] prepulse with a fraction of the intensity of the main pulse can significantly increase the soft-x-ray laser pulse energy produced by a $\lambda = 13.9$-nm Ni-like Ag laser when pumping with relatively low driving laser pulse energies [7]. In another paper this work was expanded upon to allow the generation of 4.7-μJ pulses at $\lambda = 13.9$ nm using less than 2 J of total pump laser energy [21]. In recent previous work we used a single tailored pump laser pulse to drive strong lasing in the $\lambda = 18.9$-nm transition of Ni-like Mo at 100-Hz repetition rate that resulted in an average power of 0.15 mW [19]. Here, in order to more efficiently pump the soft-x-ray amplifier plasma and allow generation at shorter wavelengths, we made use of a tailored temporal pulse profile that consists of an ~2-ns-long, low-amplitude ramp that creates and ionizes the plasma and a short-duration intense pulse that precedes the main peak of the pulse as shown in Fig. 1(b). Hydrodynamic and atomic physics plasma simulations show that the pump pulse profile, consisting of a nanosecond ramp followed by two peaks of picosecond duration, creates a plasma with an increased density of Ni-like ions at the time of maximum temperature that results in a larger gain coefficient over a temporally and spatially enlarged region leading to a threefold increase in the soft-x-ray laser output pulse energy. This increase in pumping efficiency combined with the increased repetition rate results in extremely high average power at these wavelengths from a tabletop device. Using this approach, bright lasing was also demonstrated at a number of wavelengths between 10.9 and 14.7 nm, including the high-repetition-rate, gain-saturated operation of a $\lambda = 11.9$-nm laser from Ni-like Sn. These results will enable technologic applications and basic

*brendan.reagan@colostate.edu

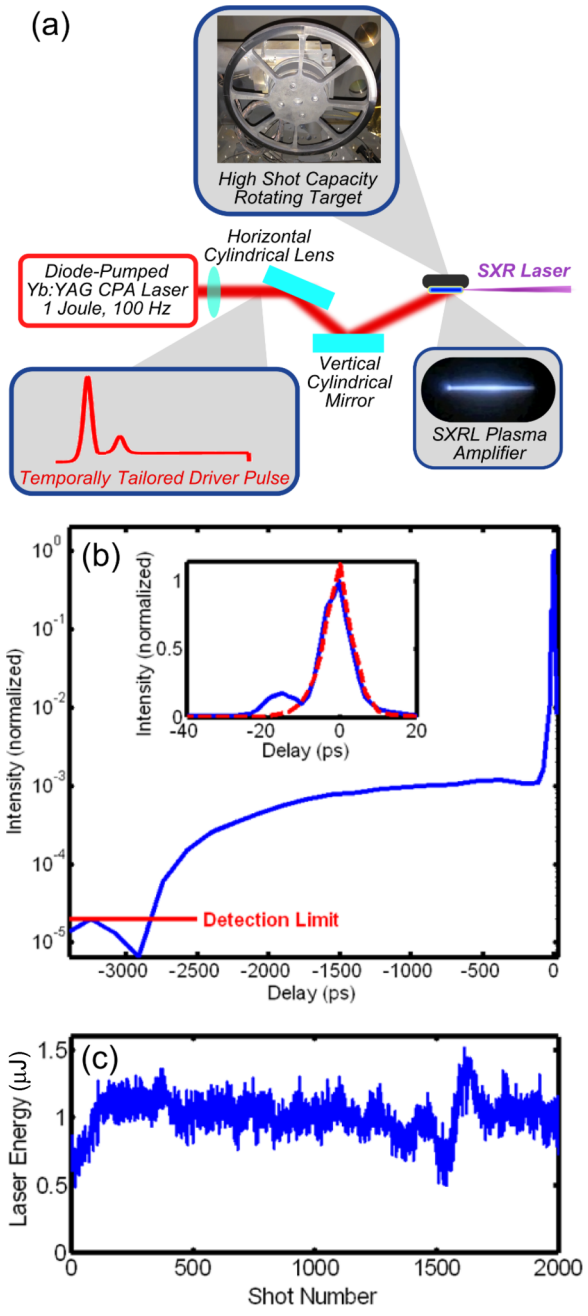

FIG. 1. (Color online) (a) Pump beam focusing and target configuration for high-repetition-rate SXR laser operation. The circular target is rotated at different selected speeds depending on the laser material. (b) Pump pulse temporal profile consisting of a long ramp ending in a sequence of two closely spaced picosecond-duration peaks. The inset is a zoom of the two short pump peaks at the end of the ramp. (c) Sequence of pulses from a 13.9-nm Ni-like Ag laser operating at 100-Hz repetition rate. The average pulse energy corresponds to an average power of 0.1 mW. The variation of the output pulse energy around shot 1500 is the result of shooting over a target region that was already irradiated.

research experiments requiring high average photon flux and open a path to further scale compact SXRLs to milliwatt average power in this wavelength range and possibly at shorter wavelengths.

II. EXPERIMENTS

A. Setup and procedures

The high-repetition-rate diode-pumped $\lambda = 1.03$-μm CPA pump laser system used to obtain the results reported here amplifies stretched pulses from a mode-locked Yb:KYW oscillator in a room-temperature Yb:YAG regenerative preamplifier and two cryogenic Yb:YAG power amplifiers operating at 100-Hz repetition rate. A dielectric grating pair compresses the pulses into 1-J pulses with durations as short as 5 ps FWHM. This CPA laser is described in Refs. [19,22,23]. After compression, the laser pulses are focused using cylindrical optics onto a solid target at a grazing incidence [15,24] angle of 32° to form a 30-μm-FWHM-wide by 5-mm-long line focus as shown in Fig. 1(a). For prolonged high-repetition-rate operation we made use of a circular target consisting of a 100-mm-diam copper disk [Fig. 1(a)] with a foil of the desired lasing material (in this case Ag or Sn) soldered to its face. The target material is mechanically polished to a smooth flat face suitable to produce an axially uniform plasma column when irradiated with the driving laser. The target is rotated using a motorized stage to present a fresh surface for each consecutive laser shot allowing for prolonged laser operation, as we previously demonstrated in [20]. Single-shot, on-axis extreme ultraviolet (EUV) plasma emission spectra were obtained using a 1200-line/mm grazing incidence, flat-field, gold-coated diffraction grating, and an x-ray-sensitive CCD. For the high-repetition-rate soft-x-ray laser measurements, an EUV-sensitive (10×1)-mm^2 silicon photodiode was placed in the imaging plane of the spectrometer at the location corresponding to the laser wavelength. Thin zirconium and Parylene filters (0.3 μm Zr and 0.1 μm Parylene) were used to reject visible plasma emission and also to prevent detector saturation. Absolute energy measurements were made using the reported efficiency of the diffraction grating, the reported responsivities of the Si photodiode and CCD, and the transmission efficiency of the thin filters measured *in situ*.

The pump pulse profile was measured via second-harmonic-generation cross correlation of the driving laser pulse with 100-μJ, 700-fs-FWHM pulses produced by a Yb:KYW regenerative amplifier. This amplifier was seeded by the same mode-locked oscillator used to seed the SXRL pump laser, allowing for simple temporal synchronization. The measurement was sensitive down to a relative intensity of $\sim 10^{-5}$, limited by the detection of stray light from the cross correlator. The presence of any non-negligible pulses before the 3.5-ns temporal window shown was ruled out by measurement with a fast photodiode. As can be seen in Fig. 1(b), the main peak of the driving laser is preceded by an intentionally added pedestal that ramps from a relative intensity of $\sim 10^{-4}$, 2.7 ns before the peak, to about 10^{-3} before the onset of the main intensity peak. This pedestal results from amplified spontaneous emission (ASE) within the first amplifier stage, with both the duration and intensity adjustable by controlling the strength of the stretched seed pulses into the amplifier and the timing of the Pockels cells within and following the amplifier. Additionally, the short picosecond peak preceding the main peak is generated by splitting the seed pulse beam from the pulse stretcher using a polarizing beam splitter and a $\lambda/2$ waveplate and subsequently recombining the beams into

a single beam with an adjustable delay before seeding the regenerative amplifier. This feature is shown with a relative intensity of 12% of the main peak and preceding that main peak by 15 ps in the inset of Fig. 1(b). Because all of the temporal features originate from within the regenerative amplifier cavity, they are collinear and share the same spatial mode profile, making this truly a single pulse and avoiding the temporal and spatial overlapping that is required when using multiple pulses to drive soft-x-ray lasers. The short-duration, early pump pulse peak has proven to be crucial in increasing the soft-x-ray laser output pulse energy, which, combined with the increase in repetition rate to 100 Hz, produces high average power.

B. Demonstration of a high-average-power laser at λ = 13.9 nm and efficient lasers down to 10.9 nm

Figure 1(c) shows the measured laser pulse energy of 2000 consecutive pulses of the $\lambda = 13.9$-nm laser operating at 100-Hz repetition rate on the $4d^1S_0 \rightarrow 4p^1P_1$ transition of Ni-like Ag obtained using the tailored pump pulse profile with the dual peak shown in Fig. 1(b). The total pump pulse energy on target was 900 mJ. The circular target described earlier, which has a width of 1 cm in the direction of the line focus axis and an outer diameter of 100 mm, was rotated at 10 deg/s, resulting in a distance between successive shots of ~90 μm at 100-Hz repetition rate. The mean SXRL pulse energy was measured to be 1.0 μJ with a shot-to-shot standard deviation of 14%, resulting in an average power of 0.1 mW.

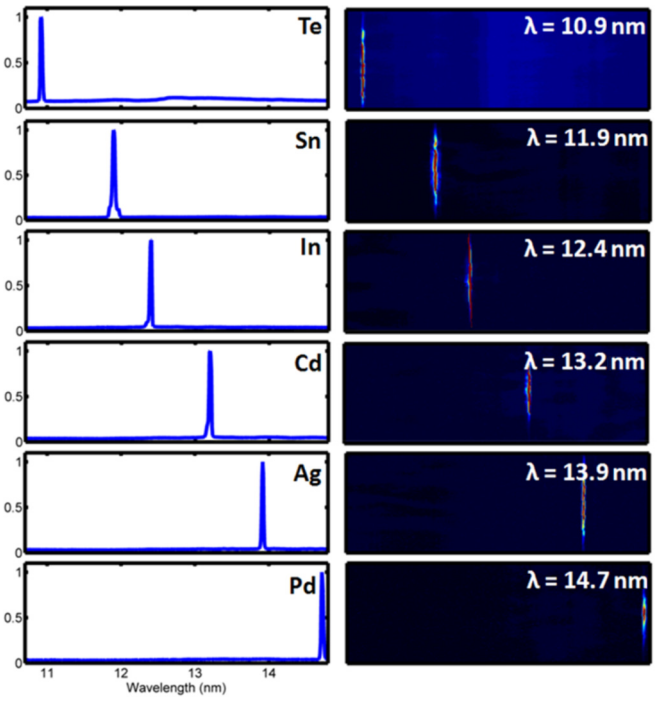

FIG. 2. (Color online) Single-shot, on-axis plasma emission spectra of $4d^1S_0 \rightarrow 4p^1P_1$ Ni-like ion soft-x-ray lasers produced by irradiating solid targets of Te, Sn, In, Cd, Ag, and Pd with a single tailored pulse of 0.9-J energy produced by a diode-pumped Yb:YAG laser. The right column shows the raw CCD image of each spectrograph. All lasers down to 11.9 nm were operated in the gain-saturated regime.

We also used the combination of the compact diode-pumped driver laser and the specially tailored driving laser pulse profile technique to demonstrate bright SXRLs at shorter wavelengths down to $\lambda = 10.9$ nm, as summarized by the single-shot on-axis spectra of Fig. 2. The same pumping geometry and detection configuration described above was employed. Rectangular slab targets were used for the case of Te, In, Cd, and Pd and a circular target of the form described above was used for Sn. For the shortest wavelength investigated, $\lambda = 10.9$ nm from Ni-like Te, the total driver laser pump energy of 0.9 J used to obtain lasing is significantly lower than that reported in previous experiments [10]. No lasing was observed when the single-peak temporal pumping profile was used with Te or Sn targets and diminished laser pulse energy was observed for Pd, Ag, Cd, and In targets.

The circular target design was used for high-repetition-rate operation of the $\lambda = 11.9$-nm Sn laser. The measurement of $\lambda =$

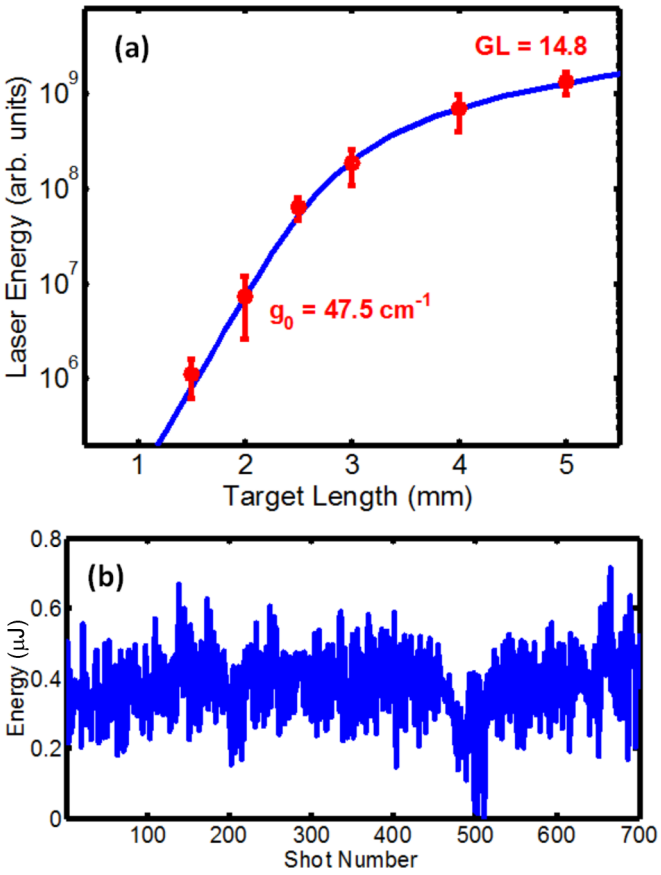

FIG. 3. (Color online) (a) Measurement of the $\lambda = 11.9$-nm Ni-like Sn laser pulse energy as a function of plasma column length. Each point is the average of five shots, with error bars representing the standard deviation of each measurement, and the solid traces show a fit of the data to the gain expression corrected for gain saturation presented in [27]. The laser is gain saturated with a small signal gain coefficient of 47.5 cm^{-1} and a gain-length product of nearly 15 for a 5-mm-long target. (b) Consecutive shots of the 11.9-nm Sn laser acquired at 50-Hz repetition rate. The mean laser pulse energy was 0.4 μJ with a standard deviation of 25%, resulting in an average power of 20 uW. The drop in energy near shot number 500 is caused by a target surface imperfection.

11.9-nm laser pulse energy as a function of target length illustrated in Fig. 3(a) shows that this SXRL laser operates in saturation for the longest target lengths with a small-signal-gain coefficient of 47.5 cm^{-1} and a gain-length product of 14.8. The total pump energy of 0.9 J employed here is less than half of that previously reported to produce gain saturation in this laser [11]. Figure 3(b) shows a sequence of 700 consecutive shots of the $\lambda = 11.9$-nm Ni-like Sn laser operating at 50-Hz repetition

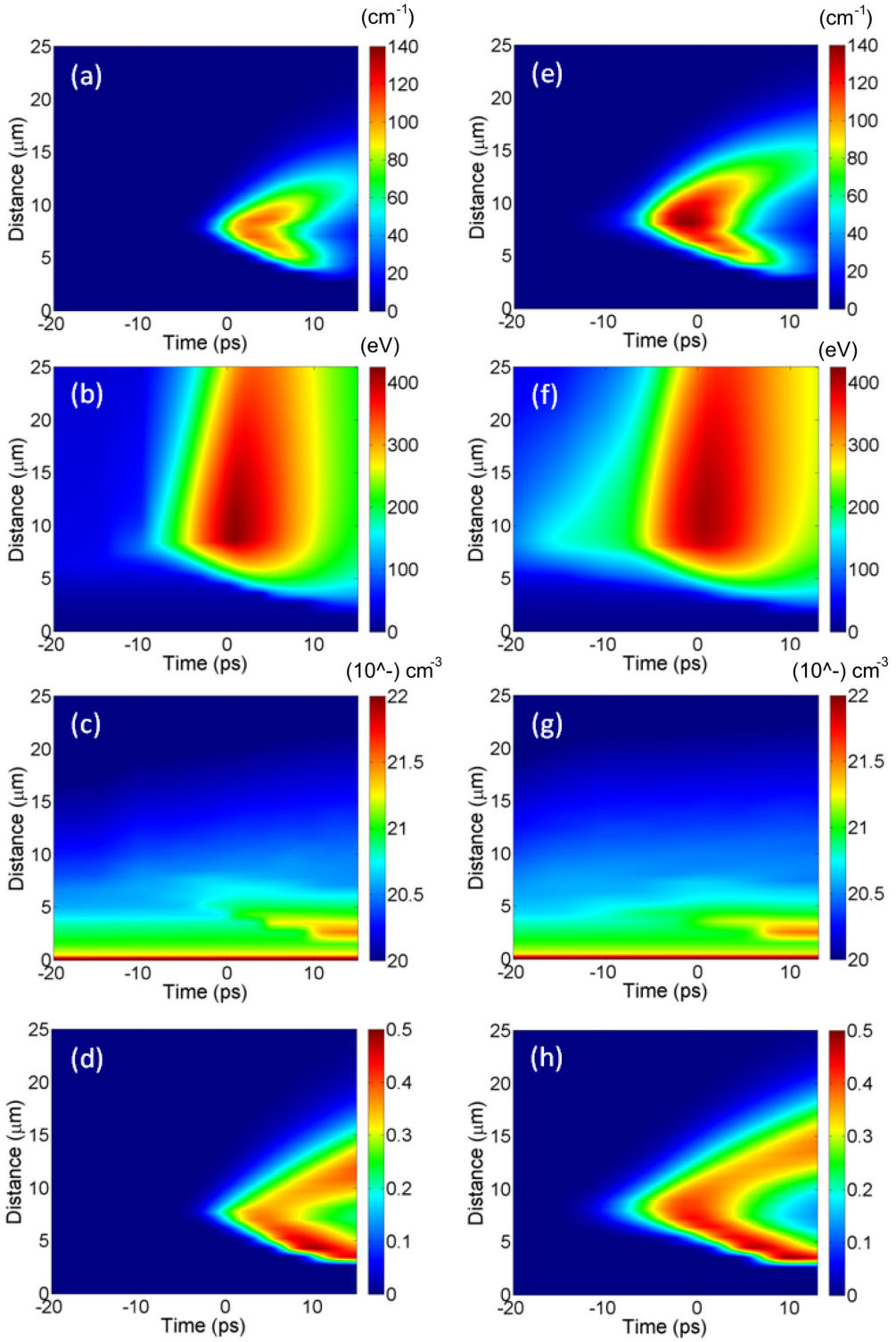

FIG. 4. (Color online) Maps of the 2D hydrodynamic simulation of the Ni-like Ag plasma created with the pulse profiles of Fig. 1(b) for (a) and (e) $\lambda = 13.9$-nm small signal gain, (b) and (f) electron temperature, (c) and (g) electron density, and (d) and (h) fraction of Ni-like ions, for the single-peak pulse profile (left column) and the dual-peak profile (right column). In all maps, the vertical scale represents the distance normal to the target and the horizontal axis is the time with $t = 0$ representing the peak of the driving laser pulse.

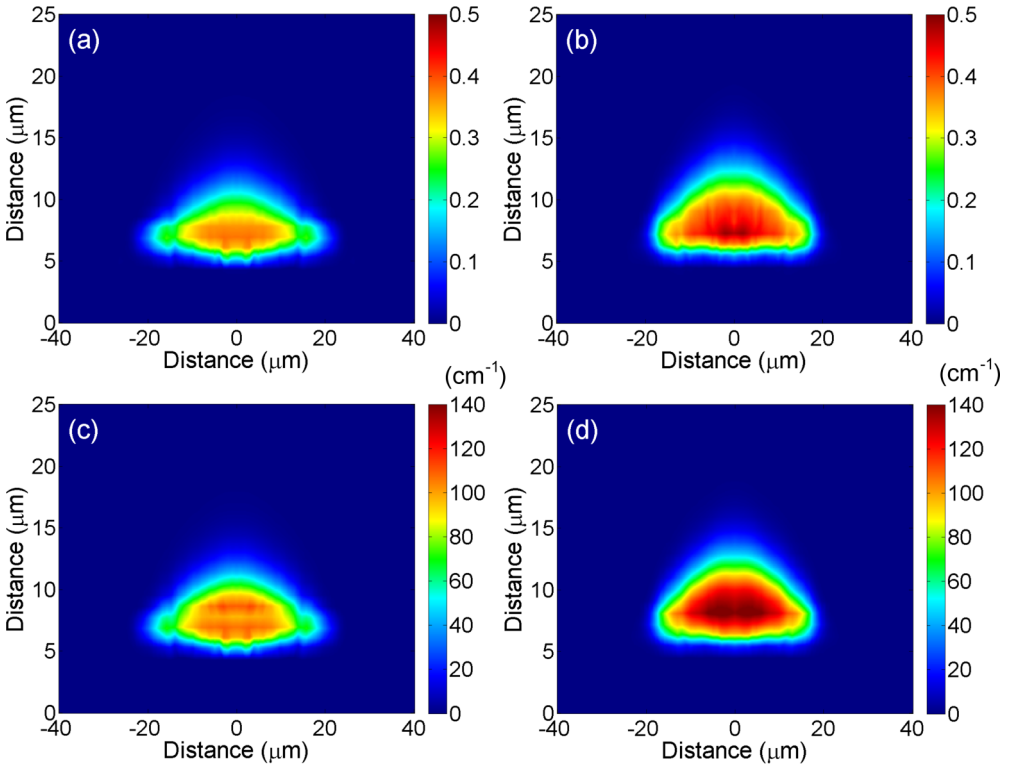

FIG. 5. (Color online) Simulated two-dimensional maps of (a) and (b) the fraction of Ni-like ions and (c) and (d) the small-signal-gain coefficient for the one-peak (left column) and two-peak (right column) pump pulse profiles. The horizontal and vertical axes represent the distances parallel and normal to the target surface, respectively. The data are plotted at the time of maximum gain, which occurs at $t = 4$ ps for the single-peak profile and at $t = -1$ ps for the dual-peak profile.

rate. The low melting point and soft nature of Sn that results in a large surface deformation by the impinging driver laser limits the maximum repetition rate to 50 Hz by the maximum available target rotation speed of 20 deg/s (~400 μm/shot). Slower target rotation speeds were observed to lead to diminished soft-x-ray laser pulse energy. The Sn SXRL laser performed at a mean pulse energy of 0.4 μJ with a shot-to-shot standard deviation of 25% resulting in an average power of 20 μW.

III. MODEL SIMULATIONS AND DISCUSSION

In order to understand the mechanisms behind the enhanced SXRL emission obtained with the ramp–dual-peak profile we simulated the laser-produced plasma amplifier with a two- dimensional (2D) hydrodynamic code with detailed atomic physics that allows the calculation of the population of all relevant energy-level populations [25]. The model results were combined with a three-dimensional ray-trace postprocessor that simulates the soft-x-ray beam generation and amplification process, allowing for direct comparison with experimental data. The atomic model solves the rate equations of ions of primary interest (lasing ions and seven neighboring ionization stages) in the fully transient approximation. The less relevant ion-state populations are computed using effective ionization and recombination rates calculated by assuming that the excited-state populations are in steady state with the ground-state populations. Each ion has atomic data from the Flexible Atomic Code (FAC) [26] with more than 10 000 levels per ion that are bundled into 20–50 effective levels. Excitation and deexcitation rates between the high-lying levels were reduced to compensate for an artificially increased ionization rate caused by the bundling or these levels. Figures 4 and 5 illustrate the model results for the $\lambda = 13.9$-nm Ni-like Ag laser under the conditions of the experiment described above. The temporal profile of the pump laser is simulated assuming a piecewise-linear interpolation of the measured temporal profiles of the driver laser pulse intensity plotted in Fig. 1(b). The line focus was approximated to be a 5-mm-long line with a width of 30-μm-FWHM Gaussian profile containing 70% of the laser pump energy in accordance with measurements obtained imaging the line focus. Computations were performed for the 32° grazing angle of incidence onto the Ag target used in the experiment. The computed plasma parameter maps of Figs. 4(a)–4(d) show the simulated $4d^1S_0 \rightarrow 4p^1P_1$ small-signal-gain coefficient, electron temperature, plasma density, and the fraction of ions in the Ni-like stage as a function of time with respect to the main peak of the pump pulse and distance from the target surface for the single-peak temporal profile. Figures 4(e)–4(h) are similar plots for the dual-peak profile. Figure 5 shows the two-dimensional model results of the small-signal gain and Ni-like fractional population at the time of maximum gain for both pulse profiles. As can be seen from these simulation results, the tailored dual-peak pump profile produces a larger gain coefficient that lasts longer in time and extends further from the target surface. This can be seen in both the 1D maps of Figs. 4(a) and 4(e) and the 2D maps of Figs. 5(c) and 5(d). The effects of the early pump pulse peak can be seen

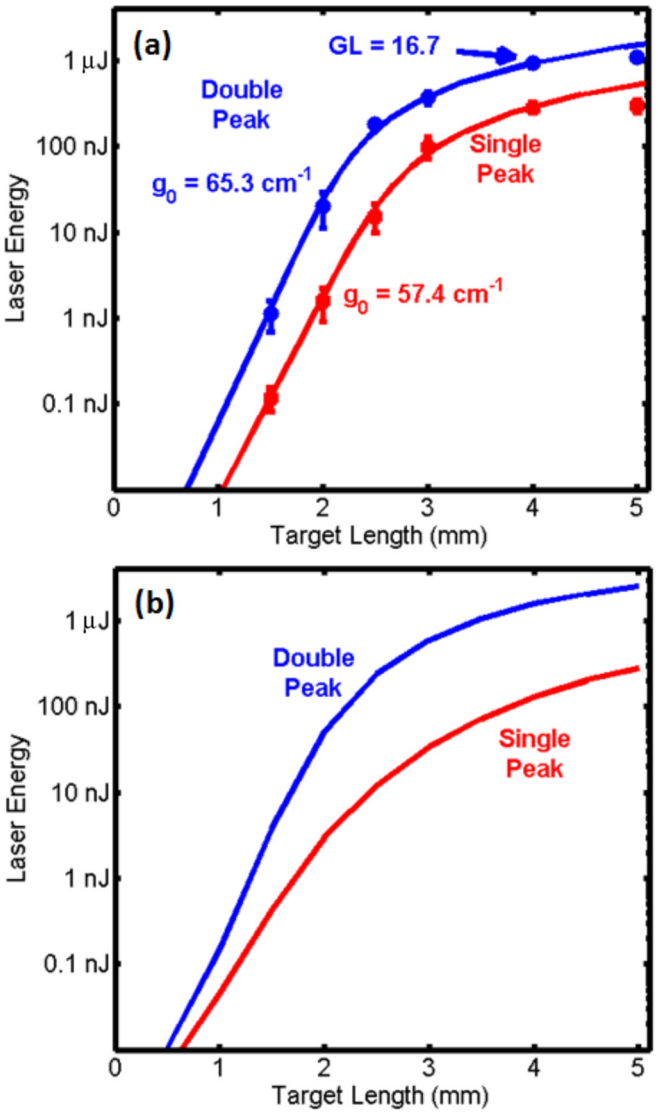

FIG. 6. (Color online) (a) Measurement of the $\lambda = 13.9$-nm Ag laser pulse energy as a function of target length for the one- and two-peak pulse profiles. The solid curves are a fit of the data to the saturated ASE laser energy expressions presented in [27]. The two-peak profile leads to a small-signal-gain coefficient of 65.3 cm^{-1} and achieved a gain-length product of $GL = 16.7$ for the 4-mm target length. The maximum of energy of about 1 μJ is about a factor of 3 higher than that obtained with the single-peak pulse profile. (b) Results of a 3D ray-trace simulation of the soft-x-ray laser energy extracted from the plasma amplifier as a function of target length using the hydrodynamic results above.

in the plasma temperature maps of Figs. 4(b) and 4(f) and in the increase of the Ni-like ion stage fractional populations of Figs. 4(h) and 5(d). The central depletion in the Ni-like ion fraction is due to overionization. The time of the maximum gain occurs at about the peak of the pump laser pulse for the two-peak profile, where the peak gain of the single-peak profile occurs several picoseconds after the pump laser peak intensity. The increase in gain occurs despite the fact that the electron temperature is about the same at the time of the main pump pulse. It is the higher electron temperature at times prior to the arrival of main pulse that creates the higher density of Ni-like ions at the time of maximum electron temperature [Figs. 4(d) and 4(h)], resulting in the larger gain. Refraction differences play only a secondary role, as the electron density profiles are not significantly different. The larger gain combined with the larger size of the gain region and a longer duration results in a significant increase in the output pulse energy.

The results of the hydrodynamic plasma model simulations were entered into a three-dimensional ray-tracing postprocessor that simulated the soft-x-ray amplification. This allows us to directly compare the experimentally measured soft-x-ray laser pulse energy as a function of plasma length with those predicted by the plasma model. The ray-trace post processor solves the propagation equation and the coupled atomic rate equations including stimulated emission. The propagation equation is solved using the ray approximation. The atomic model is the same atomic model used to calculate the gain with the addition of the stimulated emission and absorption rates. The model is fully resolved in three dimensions, frequency, and time [25]. Figures 6(a) and 6(b) show the measured and simulated $\lambda = 13.9$-nm laser pulse energies as a function of target length for both driving laser temporal profiles. As can be seen from Fig. 6(a), the laser is gain saturated for the longest target lengths with either driving laser profile. However, the dual-peak profile results in a higher small-signal gain, 65 cm^{-1} vs 57 cm^{-1}, and about a factor of 3 higher SXRL pulse energy at the longest target lengths. When fit with the expression for gain-saturated ASE given in [27], the dual-peak profile achieves a gain-length product of $GL = 16.7$ at a plasma amplifier length of 4 mm. The reasonably good agreement between the simulations and the model serves to validate the model and its conclusions. Despite the importance of the presence of the early pump pulse peak, the SXRL output is relatively insensitive to its relative intensity and delay with respect to the main pump pulse peak. Delays of 10–70 ps and relative intensities within 10%–25% of the main pump peak were experimentally observed to produce similar $\lambda = 13.9$-nm laser pulse energies, which makes this a robust system.

IV. CONCLUSION

In summary, we have demonstrated 100-Hz-repetition-rate SXRL operation with an average power of 0.1 mW at $\lambda = 13.9$ nm. A SXRL average power of 20 μW was obtained at $\lambda = 11.9$ nm operating at 50-Hz repetition rate. These results were made possible by combining a diode-driven CPA solid-state laser that produces 1-J picosecond pulses at 100-Hz repetition rate with a tailored pulse pump pulse profile for efficient pumping of the plasma amplifier. Model simulation shows that an excitation pulse consisting of a several nanoseconds ramp ending with a sequence of two shortly spaced intense picosecond peaks affects the density distribution of Ni-like ions at the time of maximum plasma temperature, producing a larger-size and longer-lasting gain region with increased gain coefficient. This results in a threefold increase in SXRL pulse energy with respect to that obtained with a simpler pump pulse consisting of a ramp and a single short peak. Additionally, the scheme was used to obtain bright lasing at several wavelengths between $\lambda = 10.9$ and 14.7 nm. The high average photon flux of these diode-pumped high-repetition-rate lasers will

enable a number of applications including defect-free coherent lithography [28] and laser nanomachining [29] with high spatial resolutions. Further scaling in repetition rate can be expected to lead to milliwatt-average-power tabletop SXRLs.

ACKNOWLEDGMENTS

The authors acknowledge the contributions of Alden H. Curtis, Federico J. Furch, Brad Luther, Brandon Carr, Anthony Nichols, Leon Durivage, and Chase Salsbury. This work was supported by the AMOS program of the Office of Basic Energy Sciences, U.S. Department of Energy and by the National Science Foundation Engineering Research Center for Extreme Ultraviolet Science and Technology using equipment developed with NSF MRI Grant No. 0521649. Optical coatings for the driver laser were developed by Dinesh Patel and Carmen S. Menoni with the support of the Office of Naval Research and the High Energy Laser Program of the Department of Defense Joint Technology Office. This research used the CSU ISTeC HPC System supported by NSF Grant No. CNS-0923386. M.B. acknowledges support for staff members at Oak Ridge National Laboratory managed by UT-Battelle, LLC, for the U.S. Department of Energy under Contract No. DE-AC05-00OR22725. Accordingly, the U.S. Government retains a nonexclusive, royalty-free license to publish or reproduce the published form of this contribution, or allow others to do so, for U.S. Government purposes.

[1] W. Ackermann *et al.*, Nat. Photon. **1**, 336 (2007).
[2] E. Allaria *et al.*, Nat. Photon. **6**, 699 (2012).
[3] M.-C. Chen, P. Arpin, T. Popmintchev, M. Gerrity, B. Zhang, M. Seaberg, D. Popmintchev, M. M. Murnane, and H. C. Kapteyn, Phys. Rev. Lett. **105**, 173901 (2010).
[4] I. Pupeza, S. Holzberger, T. Eidam, H. Carstens, D. Esser, J. Weitenberg, P. Russbuldt, J. Rauschenberger, J. Limpert, T. Udem, A. Tunnermann, T. Hansch, A. Apolonski, F. Krausz, and E. Fill, Nat. Photon. **7**, 608 (2013).
[5] S. Suckewer and P. Jaeglé, Laser Phys. Lett. **6**, 411 (2009).
[6] D. Alessi, Y. Wang, B. M. Luther, L. Yin, D. H. Martz, M. R. Woolston, Y. Liu, M. Berrill, and J. J. Rocca, Phys. Rev. X **1**, 021023 (2011).
[7] R. A. Banici, G. V. Cojocaru, R. G. Ungureanu, R. Dabu, D. Ursescu, and H. Stiel, Opt. Lett. **37**, 5130 (2012).
[8] D. H. Martz, D. Alessi, B. M. Luther, Y. Wang, D. Kemp, M. Berrill, and J. J. Rocca, Opt. Lett. **35**, 1632 (2010).
[9] D. Zimmer, B. Zielbauer, M. Pittman, O. Guilbaud, J. Habib, S. Kazamias, D. Ros, V. Bagnoud, and T. Kuehl, Opt. Lett. **35**, 450 (2010).
[10] D. Alessi, D. H. Martz, Y. Wang, M. Berrill, B. M. Luther, and J. J. Rocca, Opt. Lett. **35**, 414 (2010).
[11] M. Grünig, C. Imesch, F. Staub, and J. E. Balmer, Opt. Commun. **282**, 267 (2009).
[12] J. Goddet, S. Sebban, J. Gautier, P. Zeitoun, C. Valentin, F. Tissandier, T. Marchenko, G. Lambert, M. Ribières, D. Douillet, T. Lefrou, G. Iaquaniello, F. Burgy, G. Maynard, B. Cros, B. Robillard, T. Mocek, J. Nejdl, M. Kozlova, and K. Jakubczak Opt. Lett. **34**, 2438 (2009).
[13] H. T. Kim, I. W. Choi, N. Hafz, J. H. Sung, T. J. Yu, K.-H. Hong, T. M. Jeong, Y.-C. Noh, D.-K. Ko, K. A. Janulewicz, J. Tümmler, P. V. Nickles, W. Sandner, and J. Lee, Phys. Rev. A **77**, 023807 (2008).
[14] Y. Ochi, N. Hasegawa, T. Kawachi, and K. Nagashima, Appl. Opt. **46**, 1500 (2007).
[15] Y. Wang, M. A. Larotonda, B. M. Luther, D. Alessi, M. Berrill, V. N. Shlyaptsev, and J. J. Rocca, Phys. Rev. A **72**, 053807 (2005).
[16] B. R. Benware, C. D. Macchietto, C. H. Moreno, and J. J. Rocca, Phys. Rev. Lett. **81**, 5804 (1998).
[17] C. D. Macchietto, B. R. Benware, and J. J. Rocca, Opt. Lett. **24**, 1115 (1999).
[18] M. Frati, M. Seminario, and J. J. Rocca, Opt. Lett. **25**, 1022 (2000).
[19] B. A. Reagan, K. A. Wernsing, A. H. Curtis, F. J. Furch, B. M. Luther, D. Patel, C. S. Menoni, and J. J. Rocca, Opt. Lett. **37**, 3624 (2012).
[20] B. A. Reagan, W. Li, L. Urbanski, K. A. Wernsing, C. Salsbury, C. Baumgarten, M. C. Marconi, C. S. Menoni, and J. J. Rocca, Opt. Express **21**, 28380 (2013).
[21] G. V. Cojocaru, R. G. Ungureanu, R. A. Banici, D. Ursescu, O. Delmas, M. Pittman, O. Guilbaud, S. Kazamias, K. Cassou, J. Demailly, O. Neveu, E. Baynard, and D. Ros, Opt. Lett. **39**, 2246 (2014).
[22] A. H. Curtis, B. A. Reagan, K. A. Wernsing, F. J. Furch, B. Luther, and J. J. Rocca, Opt. Lett. **36**, 2164 (2011).
[23] B. A. Reagan, A. H. Curtis, K. A. Wernsing, F. J. Furch, B. M. Luther, and J. J. Rocca, IEEE J. Quantum Electron. **48**, 827 (2012).
[24] R. Keenan, J. Dunn, P. K. Patel, D. F. Price, R. F. Smith, and V. N. Shlyaptsev, Phys. Rev. Lett. **94**, 103901 (2005).
[25] M. Berrill, Ph.D. thesis, Colorado State University, 2010.
[26] M. F. Gu, Astrophys. J. **582**, 1241 (2003).
[27] J. Y. Lin, G. J. Tallents, J. Zhang, A. G. MacPhee, C. L. S. Lewis, D. Neely, J. Nilsen, G. J. Pert, R. M. N. O'Rourke, and R. Smith, Opt. Commun. **158**, 55 (1998).
[28] L. Urbanski, A. Isoyan, A. Stein, J. J. Rocca, C. S. Menoni, and M. C. Marconi, Opt. Lett. **37**, 3633 (2012).
[29] H. Bravo, B. T. Szapiro, P. W. Wachulak, M. C. Marconi, W. Chao, E. H. Anderson, C. S. Menoni, and J. J. Rocca, IEEE J. Sel. Top. Quantum Electron. **18**, 443 (2012).